PROCEEDINGS OF SCIENCE

Higgs production in e and γ collision

Norihisa Watanabe and Yoshimasa Kurihara
National Laboratory for High Energy Physics (KEK), Tsukuba, Ibaragi 305-0801, Japan
E-mail: norihisa@post.kek.jp, yoshimasa.kurihara@kek.jp

Tsuneo Uematsu
Institute for Liberal Arts and Sciences, Kyoto University, Kyoto 606-8501, Japan
and Maskwa Institute, Kyoto Sangyo University, Kyoto 603-8555, Japan
E-mail: uematsu@scphys.kyoto-u.ac.jp

Ken Sasaki*
Dept. of Physics, Faculty of Engineering, Yokohama National University, Yokohama 240-8501, Japan
E-mail: sasaki@ynu.ac.jp

We investigate the SM Higgs boson production in $e^-\gamma$ collision. The electroweak one-loop contributions to the scattering amplitude for $e\gamma \to eH$ are calculated and they are expressed in analytical form. We analyze the cross section for Higgs production in e-γ collision and examine the feasibility to find the Higgs boson in $e+\gamma \to e+b+\bar{b}$ channel.

11th International Symposium on Radiative Corrections (Applications of Quantum Field Theory to Phenomenology) (RADCOR 2013),
22-27 September 2013
Lumley Castle Hotel, Durham, UK

*Speaker.

PoS(RADCOR 2013)050

1. Introduction

A Higgs boson with mass about 125 GeV has been discovered by ATLAS and CMS at LHC [1] and its spin and couplings to other particles have been studied. For future detailed studies of its properties, a new accelerator facility, a linear e^+e^- collider, which offers much cleaner experimental collisions, is attracting growing attention [2]. Along with e^+e^- collider, other options such as e^-e^-, $e^-\gamma$ and $\gamma\gamma$ colliders have been also discussed [3, 4, 5]. In this talk, I report our recent study of the Standard Model (SM) Higgs boson (H) production in $e^-\gamma$ collider. We examine the reaction $e^- + \gamma \to e^- + H$ at one-loop level. Analytical expressions are obtained for the amplitude and the cross section for the Higgs production in $e\gamma$ collision is analyzed.

2. Higgs production in e-γ collision in SM

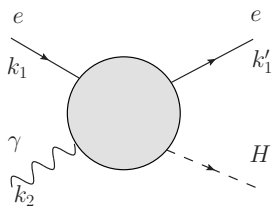

Figure 1: Higgs prodution in e-γ collision: $e\gamma \to eH$.

We examine the reaction shown in Fig.1,

$$e^-(k_1) + \gamma(k_2) \to e^-(k_1') + H(p_h) \ . \tag{2.1}$$

The relevant Feynman diagrams for this process start at the one-loop level. We calculate the relevant one-loop diagrams in unitary gauge using dimensional regularization which respects electromagnetic gauge invariance. The one-loop diagrams which contribute to the reaction (2.1) are classified into four groups: $\gamma^*\gamma$ fusion diagrams, $Z^*\gamma$ fusion diagrams, "W-ν_e" diagrams (Fig.2) and "Z-e" diagrams (Fig.3).

Since k_2 is the momentum of a real photon, we have $k_2^2 = 0$ and $k_2^\beta \varepsilon_\beta(k_2) = 0$, where $\varepsilon_\beta(k_2)$ is the photon polarization vector. Assuming that the electrons are massless so that $k_1^2 = {k_1'}^2 = 0$, we introduce the following Mandelstam variables:

$$s = (k_1 + k_2)^2 \ , \quad t = (k_1 - k_1')^2 \ , \quad u = (k_1 - p_h)^2 = m_h^2 - s - t \ . \tag{2.2}$$

3. Two-photon and Z-photon fusion diagrams

The Higgs production through fusion processes $\gamma^*\gamma \to H$ and $Z^*\gamma \to H$ is just opposite to the decay processes $H \to \gamma^*\gamma$ and $H \to Z^*\gamma$, which were discussed in Ref. [6] (see, for example, Ref.[7] for on-shell decays $H \to \gamma\gamma$ and $H \to Z\gamma$). Charged fermions and W boson contribute to the one-loop $\gamma^*\gamma$ and $Z^*\gamma$ fusion diagrams. Since the couplings of Higgs to fermions are proportional to the fermion mass, we only consider the top-quark for the charged fermion loop diagrams. The

calculation of the one-loop $\gamma^*\gamma$ fusion diagrams is similar to the one for $H \to \gamma\gamma$. Their contribution to the gauge invariant scattering amplitude for $e\gamma \to eH$ is written as follows:

$$A_{\gamma\gamma} = \Big(\frac{e^3 g}{16\pi^2}\Big)\Big[\overline{u}(k_1')\gamma_\mu u(k_1)\Big]\frac{1}{t}\Big(g^{\mu\beta} - \frac{2k_2^\mu q^\beta}{m_h^2 - t}\Big)\varepsilon_\beta(k_2) \times\Big\{\frac{2m_t^2}{m_W}N_c Q_t^2\, S^{\gamma\gamma}_{(T)}(t,m_t^2,m_h^2) - m_W S^{\gamma\gamma}_{(W)}(t,m_W^2,m_h^2)\Big\}\,, \tag{3.1}$$

where e and g are the electromagnetic coupling and the weak gauge coupling, respectively, and $N_c = 3$ and $Q_t = \frac{2}{3}$. $S^{\gamma\gamma}_{(T)}$ and $S^{\gamma\gamma}_{(W)}$ are contributions from top loops and W loops, respectively, and expressed in terms of the Passarino-Veltman two- and three-point scalar integrals B_0's and C_0 [8],

$$S^{\gamma\gamma}_{(T)}(t,m_t^2,m_h^2) = 2 + \frac{2t}{m_h^2 - t}\Big[B_0(m_h^2;m_t^2,m_t^2) - B_0(t;m_t^2,m_t^2)\Big] + \{4m_t^2 - m_h^2 + t\}C_0(m_h^2,0,t;m_t^2,m_t^2,m_t^2)\,, \tag{3.2}$$

$$\begin{aligned} S^{\gamma\gamma}_{(W)}(t,m_W^2,m_h^2) = {} & 6 + \frac{m_h^2 - t}{m_W^2} - \frac{m_h^2 t}{2m_W^4} \\ & + \frac{t\left(12m_W^4 + 2m_W^2\left(m_h^2 - t\right) - m_h^2 t\right)}{2m_W^4\left(m_h^2 - t\right)}\Big[B_0(m_h^2;m_W^2,m_W^2) - B_0(t;m_W^2,m_W^2)\Big] \\ & + \Big\{\frac{t\left(m_h^2 - 2t\right)}{m_W^2} + 12m_W^2 - 6m_h^2 + 6t\Big\}C_0(m_h^2,0,t;m_W^2,m_W^2,m_W^2)\,. \end{aligned} \tag{3.3}$$

Similar expressions appear in the decay processes $H \to \gamma\gamma$ and $H \to Z\gamma$ [6, 7], but here in Eqs.(3.2)-(3.3), t is space-like.

The one-loop $Z^*\gamma$ fusion diagrams are obtained from $\gamma^*\gamma$ fusion diagrams by replacement of the photon propagator with that of the Z boson. Their contribution is expressed as

$$A_{Z\gamma} = \Big(\frac{eg^3}{16\pi^2}\Big)\Big[\overline{u}(k_1')\gamma_\mu\Big(f_{Ze} + \gamma_5\Big)u(k_1)\Big]\frac{1}{t - m_Z^2}\Big(g^{\mu\beta} - \frac{2k_2^\mu q^\beta}{m_h^2 - t}\Big)\varepsilon_\beta(k_2) \times\Big\{-\frac{m_t^2}{8m_W\cos^2\theta_W}N_c Q_t f_{Zt} S^{Z\gamma}_{(T)}(t,m_t^2,m_h^2) + \frac{m_W}{4}S^{Z\gamma}_{(W)}(t,m_W^2,m_h^2)\Big\}, \tag{3.4}$$

where f_{Ze} and f_{Zt} are the strength of vector part of the Z coupling to electron and top quark, respectively, and are given by

$$f_{Ze} = -1 + 4\sin^2\theta_W\,, \qquad f_{Zt} = 1 - \frac{8}{3}\sin^2\theta_W\,. \tag{3.5}$$

The axial vector part of the Z coupling to top quark gives a null effect and we obtain

$$S^{Z\gamma}_{(T)}(t,m_t^2,m_h^2) = S^{\gamma\gamma}_{(T)}(t,m_t^2,m_h^2)\,, \qquad S^{Z\gamma}_{(W)}(t,m_W^2,m_h^2) = S^{\gamma\gamma}_{(W)}(t,m_W^2,m_h^2)\,. \tag{3.6}$$

4. "W-ν_e" and "Z-e" diagrams

The Feynman diagrams involving W boson and electron neutrino, which are shown in Fig.2, also contribute to the Higgs production in $e\gamma$ collision. They yield the "$W\nu_e$" amplitude which is written in the following form,

$$A^{(W\nu_e)}_{e\gamma\to eH} = \Big(\frac{eg^3}{16\pi^2}\Big)\frac{m_W}{4}\Big[\overline{u}(k_1')\, F^{(W\nu_e)}_{(e\gamma\to eH)\beta}\,(1-\gamma_5)u(k_1)\Big]\varepsilon(k_2)^\beta\,, \tag{4.1}$$

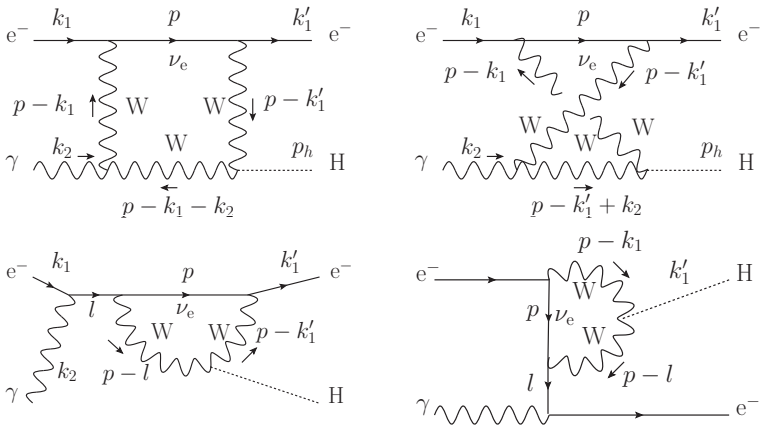

Figure 2: "W-ν_e" diagrams

where the factor $(1-\gamma_5)$ is due to the e-ν-W vertex. Thus, when the initial electron beams are right-handedly polarized, these "W-ν_e" diagrams do not contribute. The factor $F^{(W\nu_e)}_{(e\gamma\to eH)\beta}$ is written in a gauge invariant form as

$$F^{(W\nu_e)}_{(e\gamma\to eH)\beta} = \Big(\frac{2k_{1\beta}\not{k}_2}{s}-\gamma_\beta\Big)S^{(W\nu_e)(k_{1\beta})}_{(e\gamma\to eH)}(s,t,m_h^2,m_W^2)+\Big(\frac{2k'_{1\beta}\not{k}_2}{u}+\gamma_\beta\Big)S^{(W\nu_e)(k'_{1\beta})}_{(e\gamma\to eH)}(s,t,m_h^2,m_W^2), \tag{4.2}$$

where $S^{(W\nu_e)(k_{1\beta})}_{(e\gamma\to eH)}(s,t,m_h^2,m_W^2)$ and $S^{(W\nu_e)(k'_{1\beta})}_{(e\gamma\to eH)}(s,t,m_h^2,m_W^2)$ are expressed in terms of the following two-, three- and four-point scalar integrals B_0's, C_0's and D_0's,

$$\begin{aligned}
&B_0(s;0,m_W^2)\ ,\quad B_0(u;0,m_W^2)\ ,\quad B_0\left(t;m_W^2,m_W^2\right)\ ,\quad B_0\left(m_h^2;m_W^2,m_W^2\right)\ ,\\
&C_0\left(0,0,s;m_W^2,m_W^2,0\right)\ ,\quad C_0\left(0,0,u;m_W^2,m_W^2,0\right)\ ,\quad C_0\left(0,0,t;m_W^2,0,m_W^2\right)\ ,\\
&C_0\left(0,s,m_h^2;m_W^2,0,m_W^2\right)\ ,\quad C_0\left(0,u,m_h^2;m_W^2,0,m_W^2\right)\ ,\quad C_0\left(0,t,m_h^2;m_W^2,m_W^2,m_W^2\right)\ ,\\
&D_0\left(0,0,0,m_h^2;s,t;m_W^2,m_W^2,0,m_W^2\right)\ ,\quad D_0\left(0,0,0,m_h^2;t,u;m_W^2,0,m_W^2,m_W^2\right)\ .
\end{aligned} \tag{4.3}$$

With help of the results of Refs.[9, 10, 11], these scalar integrals are expressed in analytical form [12].

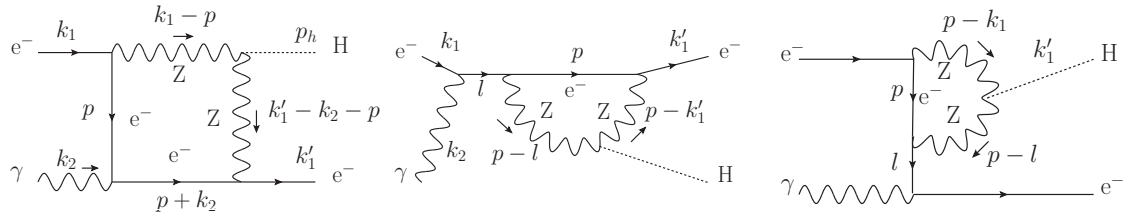

Figure 3: "Z-e" diagrams

The last one-loop contribution to the Higgs production in e and γ collision come from the Feynman diagrams shown in Fig.3. These "Z-e" diagrams give the following amplitude,

$$A^{(Ze)}_{e\gamma\to eH} = \Big(\frac{eg^3}{16\pi^2}\Big)\Big(-\frac{m_Z}{16\cos^3\theta_W}\Big)\times\Big[\bar{u}(k_1')\,F^{(Ze)}_{(e\gamma\to eH)\beta}\,(f_{Ze}+\gamma_5)^2u(k_1)\Big]\varepsilon(k_2)^\beta, \tag{4.4}$$

where the factor $(f_{Ze}+\gamma_5)^2$ arises from the Z boson coupling to electrons. The factor $F^{(Ze)}_{(e\gamma\to eH)\beta}$ is written in a gauge invariant form as

$$F^{(Ze)}_{(e\gamma\to eH)\beta} = \Big(\frac{2k_{1_\beta}\not{k}_2}{s}-\gamma_\beta\Big)S^{(Ze)(k_{1_\beta})}_{(e\gamma\to eH)}(s,t,m_h^2,m_Z^2)+\Big(\frac{2k'_{1_\beta}\not{k}_2}{u}+\gamma_\beta\Big)S^{(Ze)(k'_{1_\beta})}_{(e\gamma\to eH)}(s,t,m_h^2,m_Z^2), \quad (4.5)$$

where $S^{(Ze)(k_{1_\beta})}_{(e\gamma\to eH)}(s,t,m_h^2,m_Z^2)$ and $S^{(Ze)(k'_{1_\beta})}_{(e\gamma\to eH)}(s,t,m_h^2,m_Z^2)$ are expressed in terms of the following two-, three- and four-point scalar integrals B_0's, C_0's and D_0's [12],

$$\begin{aligned}
&B_0(s;0,m_Z^2)\ , \quad B_0(u;0,m_Z^2)\ , \quad B_0\left(m_h^2;m_Z^2,m_Z^2\right)\ ,\\
&C_0\left(0,0,s;m_Z^2,0,0\right)\ , \quad C_0\left(0,0,u;m_Z^2,0,0\right)\ , \quad C_0\left(0,s,m_h^2;m_Z^2,0,m_Z^2\right)\ , \quad C_0\left(0,u,m_h^2;m_Z^2,0,m_Z^2\right)\ ,\\
&D_0\left(0,0,0,m_h^2;s,u;m_Z^2,0,0,m_Z^2\right)\ . \qquad (4.6)
\end{aligned}$$

Collinear singularities arise in the tree-point integrals $C_0\left(0,0,s;m_Z^2,0,0\right)$, $C_0\left(0,0,u;m_Z^2,0,0\right)$, and four-point integral $D_0\left(0,0,0,m_h^2;s,u;m_Z^2,0,0,m_Z^2\right)$. But these three scalar integrals appear in combination and, in the end, their collinear divergences cancel out. Thus $S^{(Ze)(k_{1_\beta})}_{(e\gamma\to eH)}(s,t,m_h^2,m_Z^2)$ and $S^{(Ze)(k'_{1_\beta})}_{(e\gamma\to eH)}(s,t,m_h^2,m_Z^2)$ are both finite. The analytical expressions of the scalar integrals given in Eq.(4.6) will be reported elsewhere [12].

5. Numerical Analysis

Using the results obtained in Sec.3-4, we analyze numerically the Higgs production cross section in unpolarized e and γ collision. Taking the average over initial electron and photon polarizations, we obtain for the differential cross section,

$$\frac{d\sigma^{\rm all}_{e\gamma\to eH}}{dt} = \frac{1}{16\pi s^2}\times\left\{\frac{1}{4}\sum_{\rm polarization}|A|^2\right\}, \quad (5.1)$$

where $A = A_{\gamma\gamma}+A_{Z\gamma}+A^{(W\nu_e)}_{e\gamma\to eH}+A^{(Ze)}_{e\gamma\to eH}$.

In order to see the relative contributions from $\gamma^*\gamma$ fusion, $Z^*\gamma$ fusion, "W-ν_e" and "Z-e" diagrams, we evaluate the differential cross section given in Eq.(5.1) replacing A with $A_{\gamma\gamma}, A_{Z\gamma}, A^{(W\nu_e)}_{e\gamma\to eH}$ and $A^{(Ze)}_{e\gamma\to eH}$, respectively, and obtain

$$\frac{d\sigma_{(\gamma\gamma\ \text{fusion})}}{dt} = \frac{1}{16\pi s^2}\Big(\frac{e^3 g}{16\pi^2}\Big)^2\Big(-\frac{1}{t}\Big)\frac{s^2+u^2}{(m_h^2-t)^2}\left|\frac{2m_t^2}{m_W}N_c Q_t^2\ S^{\gamma\gamma}_{(T)}(t,m_t^2,m_h^2)-m_W S^{\gamma\gamma}_{(W)}(t,m_W^2,m_h^2)\right|^2, \quad (5.2)$$

$$\begin{aligned}
\frac{d\sigma_{(Z\gamma\ \text{fusion})}}{dt} &= \frac{1}{16\pi\ s^2}\Big(\frac{eg^3}{16\pi^2}\Big)^2(f_{Ze}^2+1)\frac{-t}{(t-m_Z^2)^2}\frac{s^2+u^2}{(m_h^2-t)^2}\\
&\quad\times\left|-\frac{m_t^2}{8m_W\cos^2\theta_W}N_c Q_t f_{Zt}S^{\gamma\gamma}_{(T)}(t,m_t^2,m_h^2)+\frac{m_W}{4}S^{\gamma\gamma}_{(W)}(t,m_W^2,m_h^2)\right|^2, \quad (5.3)
\end{aligned}$$

$$\frac{d\sigma^{(W\nu_e)}_{(e\gamma\to eH)}}{dt} = \frac{1}{16\pi s^2}\Big(\frac{eg^3}{16\pi^2}\Big)^2\frac{m_W^2}{8}(-t)\left\{\left|S^{(W\nu_e)(k_{1_\beta})}_{(e\gamma\to eH)}(s,t,m_h^2,m_Z^2)\right|^2+\left|S^{(W\nu_e)(k'_{1_\beta})}_{(e\gamma\to eH)}(s,t,m_h^2,m_Z^2)\right|^2\right\}, \quad (5.4)$$

$$\begin{aligned}
\frac{d\sigma^{(Ze)}_{(e\gamma\to eH)}}{dt} &= \frac{1}{16\pi s^2}\Big(\frac{eg^3}{16\pi^2}\Big)^2\Big(\frac{m_Z}{16\cos^3\theta_W}\Big)^2(f_{Ze}^4+6f_{Ze}^2+1)(-t)\\
&\quad\times\left\{\left|S^{(Ze)(k_{1_\beta})}_{(e\gamma\to eH)}(s,t,m_h^2,m_Z^2)\right|^2+\left|S^{(Ze)(k'_{1_\beta})}_{(e\gamma\to eH)}(s,t,m_h^2,m_Z^2)\right|^2.\right\} \quad (5.5)
\end{aligned}$$

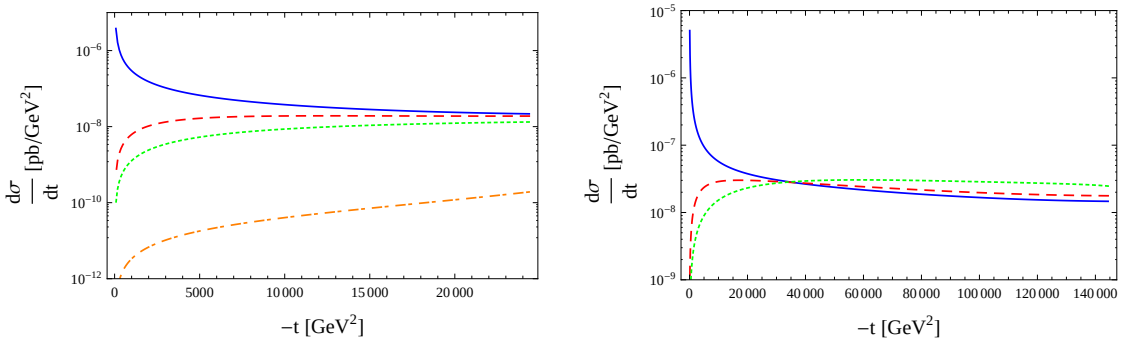

Figure 4: Differential cross sections $d\sigma_{(\gamma\gamma \text{ fusion})}/dt$ (blue solid line), $d\sigma_{(Z\gamma \text{ fusion})}/dt$ (red dashed line), $d\sigma^{(W\nu_e)}_{(e\gamma\to eH)}/dt$ (green dotted line) and $d\sigma^{(Ze)}_{(e\gamma\to eH)}/dt$ (orange dashed dotted line) as functions of t for the cases (a) $\sqrt{s} = 200$GeV and (b) $\sqrt{s} = 400$GeV. In the plot (b), $d\sigma^{(Ze)}_{(e\gamma\to eH)}/dt$ is too small and is out of the plot range.

We plot $\frac{d\sigma_{(\gamma\gamma \text{ fusion})}}{dt}$, $\frac{d\sigma_{(Z\gamma \text{ fusion})}}{dt}$, $\frac{d\sigma^{(W)}_{(e\gamma\to eH)}}{dt}$ and $\frac{d\sigma^{(Z)}_{(e\gamma\to eH)}}{dt}$ as functions of t in Fig.4 for the cases (a) $\sqrt{s} = 200$GeV and (b) $\sqrt{s} = 400$GeV. We choose the mass parameters and the coupling constants as follows: $m_h = 125$ GeV, $m_t = 173$ GeV, $m_Z = 91$ GeV, $m_W = 80$ GeV, $\cos\theta_W = m_W/m_Z$, $g = e/\sin\theta_W$, and e^2 is chosen to be the value at the scale of m_Z, i.e., $e^2 = 4\pi/128$. We see from Fig.4 (a) and (b) that a dominant contribution comes from the $\gamma^*\gamma$ fusion diagrams for smaller t, more specifically, $t \leq (100\text{GeV})^2$. This is due to the factor $(-1/t)$ in the expression (5.2) for $d\sigma_{(\gamma\gamma \text{ fusion})}/dt$, which arises as $(-t)\times(1/t^2)$ with $1/t^2$ coming from the photon propagator. At large t, say around $t = (200\text{GeV})^2$, the differential cross sections for $\gamma^*\gamma$ fusion, $Z^*\gamma$ fusion and "W-ν_e" diagrams become the same order, and, at $t > (200\text{GeV})^2$, $d\sigma^{(W\nu_e)}_{(e\gamma\to eH)}/dt$ prevails over the other two. On the other hand, Fig.4 (a) shows that $d\sigma^{(Ze)}_{(e\gamma\to eH)}/dt$ is neglegibly small compared with the other three differential cross sections. In Fig.4 (b), it is too small to appear within the range of the plot.

Integrating the differential cross sections given in Eqs.(5.1) - (5.5) over t, we obtain the Higgs production cross section $\sigma^{\text{all}}_{e\gamma\to eH}$ in e-γ collision and each contribution from $\gamma^*\gamma$ fusion, $Z^*\gamma$ fusion, "W-ν_e" and "Z-e" diagrams. The results are plotted in Fig.5 as functions of $\sqrt{s}$. We see that, up to $\sqrt{s} \leq 400$GeV, the dominant contribution to $\sigma^{\text{all}}_{e\gamma\to eH}$ comes from $\gamma^*\gamma$ fusion diagrams. Actually, below $\sqrt{s} = 300$GeV, the contributions from $Z^*\gamma$ fusion, "W-ν_e" and "Z-e" diagrams can be negligible. On the other hand, the contributions from $\gamma^*\gamma$ fusion, $Z^*\gamma$ fusion and "W-ν_e" diagrams become the same order above $\sqrt{s} = 500$GeV.

The high-intensity γ beam can be produced by laser light backward scattering off the high energy electron beam, $e^-\gamma_{\text{Laser}} \to e^-\gamma$, where the backward-scattered photon receives a major fraction of the incoming electron energy [13]. Its energy distribution depends on the polarization of the initial electron beam (P_e) and laser photon (P_l). Assuming, for simplicity, the head-on collision of the laser photon with energy 2.33 eV and the electron beam with 250 GeV, we calculate the energy distribution of the scattered photon with different polarization configurations of the initial beams. The results are shown in Fig. 6(a). A large portion of the electron energy can be transfered to the scattered photon and the most peaked spectrum is obtained when $P_eP_l = -1$.

Then we examine the feasibility of finding the SM Higgs boson in $e+\gamma \to e+b+\bar{b}$ channel.

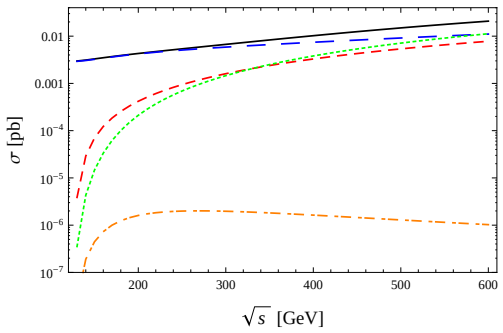

Figure 5: Higgs production cross sections $\sigma^{\rm all}_{e\gamma\to eH}$ (black solid line), $\sigma_{(\gamma\gamma\ \rm fusion)}$ (blue long dashed line), $\sigma_{(Z\gamma\ \rm fusion)}$ (red dashed line), $\sigma^{(W)}_{(e\gamma\to eH)}$ (green dotted line) and $\sigma^{(Z)}_{(e\gamma\to eH)}$ (orange dash dotted line) as functions of $\sqrt{s}$.

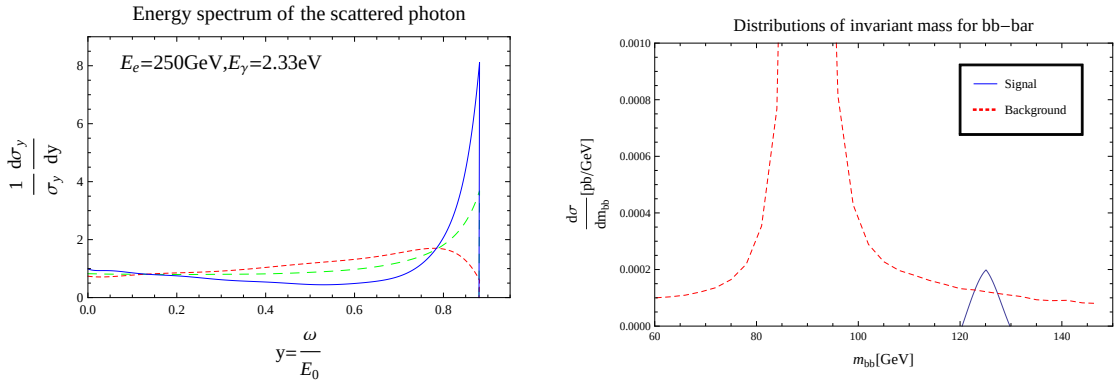

Figure 6: (a) The polarization dependent energy spectra of the scattered photon as functions of $y = \frac{\omega}{E_0}$, where ω is the energy of the scattered photon and $E_0 = 250$ GeV. The red dotted, green dashed and blue solid curves represent spectra when the initial electron beam and laser photon are unpolarized ($P_eP_l = 0$), have same helicities ($P_eP_l = 1$) and different helicities ($P_eP_l = -1$), respectively; (b) The plot of $d\sigma(e+\gamma\to e+b+\bar{b})/dm_{b\bar{b}}$ for the case when the electron beam energy is 250 GeV and the photon beam has the energy spectrum expressed by the blue solid curve in the left graph.

Using the photon energy spectrum given in Fig.6(a) for the case $P_eP_l = -1$ (blue solid curve) and the results in Sec.3-4, we use GRACE and numerically calculate $d\sigma(e+\gamma\to e+b+\bar{b})/dm_{b\bar{b}}$ for the case with electron beam energy 250 GeV. The main background to the Higgs boson signal comes from the reaction $e+\gamma\to e+Z^*\to e+b+\bar{b}$. The kinematical cut of the scattered electron and b quark are chosen as $10^\circ \le \theta_{e^-} \le 170^\circ$ and $40^\circ \le \theta_b \le 170^\circ$, respectively. The result is shown in Fig.6(b) from which we see that the signals for the Higgs boson are well expected to be found. More details of the analysis will be reported elsewhere [12].

6. Summary

We have investigated the SM Higgs boson production in $e^-\gamma$ collision. The electroweak one-loop contributions to the scattering amplitude for $e\gamma\to eH$ were calculated and they are expressed

in analytical form. Then the cross section for Higgs production $\sigma^{\rm all}_{e\gamma\to eH}$ in e-γ collision was analyzed. It is found that (i) the contribution to $\sigma^{\rm all}_{e\gamma\to eH}$ from $\gamma^*\gamma$ fusion diagrams is dominant for $\sqrt{s} < 400$GeV; (ii) the contributions from $\gamma^*\gamma$ fusion, $Z^*\gamma$ fusion and "W-ν_e" diagrams become the same order above $\sqrt{s} = 500$GeV; (iii) the contributions from "Z-e" diagrams is extremely small and can be negligible. Finally, the feasibility to find the Higgs boson in $e\gamma$ collision was studied in $e+\gamma \to e+b+\bar{b}$ channel.

I thank the organizers of RADCOR 2013 for the pleasant atmosphere during the symposium.

References

[1] ATLAS Collaboration, Phys. Lett. **B716** (2012) 1-29; CMS Collaboration, Phys. Lett. **B716** (2012) 30-61.

[2] http://www.linearcollider.org/cms.

[3] A. De Roeck, "Physics at a $\gamma\gamma$, $e\gamma$ and e^-e^- Option for a Linear Collider", arXiv:hep-ph/0311138 (2003).

[4] S. A. Bogacz et al., "SAPPHiRE: a Small $\gamma\gamma$ Higgs Factory", arXiv:1208.2827 [physics.acc-ph] (2012).

[5] I. F. Ginzburg and M. Krawczyk, "Testing Higgs Physics at the Photon Collider", arXiv:1310.5881 [hep-ph] (2013).

[6] J. C. Romao and S. Andringa, Eur. Phys. J. **C 7** (1999) 631.

[7] J. F. Gunion, H. E. Haber, G. Kane and S. Dawason, "The Higgs Hunter's Guide"(Addison-Wesley, 1990).

[8] G. Passarino and M. Veltman, Nucl. Phys. **B160** (1979) 151.

[9] A. Denner, U. Nierste and R. Scharf, Nucl. Phys. **B367** (1991) 637.

[10] R.K. Ellis and G. Zanderighi, JHEP **0802** (2008) 002.

[11] A. Denner and S. Dittmaier, Nucl. Phys. **B844** (2011) 199.

[12] N. Watanabe, Y. Kuriharam, T. Uematsu and K. Sasaki, in preparation.

[13] I. F. Ginzburg, G. L. Kotkin, V. G. Serbo, and V. I. Telnov, Nucl. Instr. and Meth. **205** (1983) 47; I. F. Ginzburg et al., Nucl. Instr. and Meth. **219** (1984) 5; V. I. Telnov, Nucl. Instr. and Meth. **A294** (1990) 72; V. I. Telnov, Nucl. Instr. and Meth. **A355** (1995) 3.